Pergamon

Int. J. Heat Mass Transfer. Vol. 39, No. 6, pp. 1243–1255, 1996

0017–9310/96 $15.00+0.00

0017–9310(95)00193–X

Transient three-dimensional convection of air in a differentially heated rotating cubic cavity

T. L. LEE and T. F. LIN
Department of Mechanical Engineering, National Chiao Tung University, Hsinchu, Taiwan,
Republic of China

(*Received* 21 *April* 1994 *and in final form* 26 *May* 1995)

Abstract—Transient three-dimensional mixed convection of air in a differentially heated vertical cubic cavity rotating about a vertical axis through the cavity center is numerically investigated. The unsteady Navier–Stokes and energy equations were discretized by the power-law scheme and solved by the projection method. Results were obtained for the thermal and rotational Rayleigh and Taylor numbers all varied from 10^2 to 10^7. Effects of the centrifugal and Coriolis forces on the thermal buoyancy driven flow were examined in detail. Significant flow modification was noted when $Ra_\omega > Ra$ or $Ta > Ra$. It was noted in a rotational buoyancy dominated flow that after the initial transient the main flow structure is characterized by a symmetric pair of longitudinal rolls with their axes parallel with the rotating axis of the cavity. The increase in the Coriolis force decelerates the flow near the walls and reduces the heat transfer. The local Nusselt number distributions on the hot and cold plates were more sensitive to the change in the driving forces than the space average Nusselt numbers.

1. INTRODUCTION

Natural convection in a differentially heated non-rotating enclosed space is often encountered in various technological applications such as solar energy collection, cooling of microelectronic equipments, growing of single crystal from fluid phase, etc. It has been extensively studied and the detailed flow and thermal structures under various conditions are available in the literature. In the crystal growth application, the crucible is sometimes rotated to stabilize the buoyancy induced flow so that the growing crystal is of higher quality. As the enclosure is rotated, the flow in it is simultaneously affected by the Coriolis and centrifugal forces as well as the thermal buoyancy. The resulting flow is expected to be rather complicated and is still poorly understood.

In the past considerable attention was paid to the rotating Rayleigh–Bénard convection [1–7], that is, the convection in an infinite bounded horizontal layer of fluid subject to an unstable vertical temperature gradient, which rotates at constant angular speed about a vertical axis. From linear stability analysis for a high rotating speed, Niler and Bisshopp [1] noted that in the limit of large Taylor number, Ta, the viscous effects play an important role in a thin layer near the boundary and the critical Rayleigh number, Ra_c, for the onset of convection is independent of whether the boundaries are rigid or free. Numerical analysis conducted by Veronis [2] indicated that the Prandtl number exhibits significant effects on the flow and thermal structures. For the limit of infinite Prandtl number, Küppers and Lortz [3] showed that no stable steady-state convective flow exists if the Taylor number exceeds a certain critical value. Rossby [4] experimentally observed the subcritical instability in a water layer for $Ta > 5 \times 10^4$ and in an air layer for $Ta < 10^5$. In addition, for water at $Ra > 10^4$ the Nusselt number was found to increase with the Taylor number. The opposite trend is the case for air. Besides, at a large Taylor number oscillatory convection is preferred in mercury. Based on the mean-field approximation, Hunter and Riahi [5] analytically showed the non-monotonic variation of the Nusselt number with the Taylor number. Linear stability analysis from Rudraiah and Chandna [6] indicated that the critical Rayleigh number was relatively sensitive to the method and rate of heating, Coriolis force and the nature of the bounding surfaces of the fluid layer. The analysis from Clever and Busse [7] suggests that the critical Rayleigh number for the onset of oscillatory motion is higher for the higher Taylor and Prandtl numbers.

Another geometry of considerable interest is the flow in a bottom heated vertical closed circular cylinder rotating about its axis. Experiments for silicone oil carried out by Hudson and his coworkers [8, 9] indicated that the Nusselt number increases with the rotation rate. Steady axisymmetric numerical simulation was conducted by Chew [10]. The onset of steady natural convection was shown by Buell and Catton [11] to be rather sensitive to the lateral thermal boundary condition. Pfotenhauer *et al.* [12] reported experimental results for the effects of the cylinder geometry on the onset of convection for the low temperature liquid helium. For water subject to the Rayleigh number ranging from 10^6 to 2×10^{11} and Taylor number from 10^6 to 10^{12}, Boubnov and Golitsyn [13] experimentally observed a ring pattern of convective flow resulting from the fluid spin-up and vertex inter-

NOMENCLATURE

g	magnitude of gravity acceleration
$\mathbf{g}$	gravitational acceleration vector
H	the length of the cavity
i, j, k	indices in the X, Y, Z directions
m	number of iterations
n	index of time step
Nu	local Nusselt number
$\overline{Nu}$	space average Nusselt number
P	dimensionless pressure
p	thermodynamic pressure
Pr	Prandtl number, ν/α
p_m	dimensional modified dynamic pressure
Ra	Rayleigh number, $g \cdot \beta \cdot \Delta T \cdot H^3/(\nu\alpha)$
Ra_ω	rotational Rayleigh number, $\Omega^2 H \cdot \beta \cdot \Delta T \cdot H^3/(\nu\alpha)$
T	temperature
Ta	Taylor number, $\Omega^2 \cdot H^4/\nu^2$
T_H	temperature of the hot wall
T_L	temperature of the cold wall
T_0	initial fluid temperature, $T_0 = 0.5 \cdot (T_H + T_L)$
t, τ	dimensional and dimensionless time
U, V, W	dimensionless velocities in X, Y, Z directions
U^*, V^*, W^*	dimensionless provisional velocities in X, Y, Z directions
V_{max}	dimensionless projected velocity magnitude on the selected plane
$\mathbf{V}$	dimensionless velocity vector
u, v, w	dimensional velocities in x, y, z directions
X, Y, Z	dimensionless coordinate systems
x, y, z	dimensional coordinate systems.

Greek symbols

α	thermal diffusivity
β	thermal expansion coefficient
ΔT	temperature difference between the hot and cold walls
ν	kinematic viscosity
Ω	magnitude of angular rotation rate
$\mathbf{\Omega}$	vector of angular rotation
θ	dimensionless temperature
ρ_0	air density at temperature T_0.

actions between two adjacent vortices. Kirdyashkin and Distanov [14] found that a periodically changing rotation speed can result in periodical temperature changes throughout the entire liquid layer. The effects of the rotation on the natural convection in a vertical annulus with differentially heated vertical side walls were examined in detail by Busse and his colleagues [15–18]. Their results are relevant to the processes in stars and in the earth's core. In order to study the flow phenomena in a closed thermosyphons, steady three-dimensional free convection inside a long vertical rotating porous box with the bottom surface heated has been numerically studied by Zhao and Lock [19]. The effects of the thermal Rayleigh, rotating Rayleigh and Taylor numbers were examined.

Experimental data for the Nusselt number in a top heated horizontal rectangular cavity of silicone oil rotating about a vertical axis passing through the center of the cavity were presented by Abell and Hudson [20]. Hathaway and Somerville [21] conducted a three-dimensional and unsteady numerical simulation of an inclined rotating layer with the rotation vector tilted from the vertical. The tilting of the rotation vector was found to produce significant change in the flow structure. A combined theoretical, numerical and experimental study was presented by Bühler and Oertel [22] to investigate thermal convection in rotating rectangular shallow box heated from below. First, linear stability analysis was used to predict the onset of steady and oscillatory convection and three-dimensional flow configuration. Then, the numerical analysis predicted the change of the roll orientation with the Taylor number. Finally, the flow structures at various Rayleigh and Taylor numbers were visualized. Unusual flow circulation was experimentally observed by Condie and Griffiths [23] for a horizontal layer of water.

The above literature review indicates that the early studies mainly focused on the effects of the rotation on the onset of convection and the overall heat transfer at supercritical Rayleigh numbers. The detailed processes on how the Coriolis and centrifugal forces affect the natural convection flow structure in differentially heated cavities are still not well understood. In this study, a transient three-dimensional numerical simulation will be carried out to enhance our understanding on the rotating cavity flow. Attention will be paid to the effects of the Coriolis and centrifugal forces on the flow dominated by the thermal buoyancy, which receives relatively little attention in the literature.

2. MATHEMATICAL MODELING AND SOLUTION METHOD

2.1. *Mathematical model*

The schematic diagram of the physical system under investigation is depicted in Fig. 1. Initially at time $t < 0$, the vertical cubic cavity and inside air are both stationary and isothermal at T_0. At $t \geqslant 0$ the cavity is rotated at a constant angular speed Ω about an axis which is parallel with the side walls and is through the center of the cavity. Meanwhile, two opposite side walls are suddenly raised and lowered, respectively, to

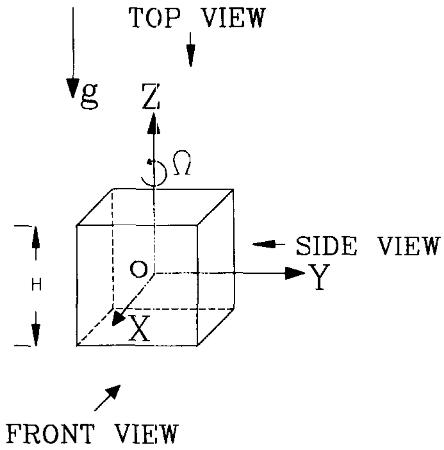

Fig. 1. Schematic diagram of the physical system.

two different but uniform temperatures $T_0+\Delta T/2$ and $T_0-\Delta T/2$, while the other walls are thermally well insulated. Thus, the air flow inside the cavity is simultaneously driven by the rotation and thermal buoyancies. By adopting the generalized Boussinesq approximation [24] in which the linear density variation with temperature is considered in both the body force and centrifugal force terms, the thermal and rotational buoyancies and Coriolis force acting onto the flow are, respectively, equal to $\rho_0 g\beta(T-T_0)$, $-\rho_0\beta(T-T_0)\mathbf{\Omega}\times(\mathbf{\Omega}\times\mathbf{r})$ and $-2\rho_0\mathbf{\Omega}\times\mathbf{V}$. The resulting flow development can be described as follows:

$$\frac{\partial u}{\partial x}+\frac{\partial v}{\partial y}+\frac{\partial w}{\partial z}=0 \tag{1}$$

$$\frac{\partial u}{\partial t}+u\frac{\partial u}{\partial x}+v\frac{\partial u}{\partial y}+w\frac{\partial u}{\partial z}$$
$$=-\frac{1}{\rho}\frac{\partial p_{\mathrm{m}}}{\partial x}+\nu\nabla^2 u+2\Omega v-\Omega^2 x\beta(T-T_0) \tag{2}$$

$$\frac{\partial v}{\partial t}+u\frac{\partial v}{\partial x}+v\frac{\partial v}{\partial y}+w\frac{\partial v}{\partial z}$$
$$=-\frac{1}{\rho}\frac{\partial p_{\mathrm{m}}}{\partial y}+\nu\nabla^2 v-2\Omega u-\Omega^2 y\beta(T-T_0) \tag{3}$$

$$\frac{\partial w}{\partial t}+u\frac{\partial w}{\partial x}+v\frac{\partial w}{\partial y}+w\frac{\partial w}{\partial z}$$
$$=-\frac{1}{\rho}\frac{\partial p_{\mathrm{m}}}{\partial z}+\nu\nabla^2 w+g\cdot\beta(T-T_0) \tag{4}$$

$$\frac{\partial T}{\partial t}+u\frac{\partial T}{\partial x}+v\frac{\partial T}{\partial y}+w\frac{\partial T}{\partial z}=\alpha\nabla^2 T \tag{5}$$

where

$$\nabla^2=\frac{\partial^2}{\partial X^2}+\frac{\partial^2}{\partial Y^2}+\frac{\partial^2}{\partial Z^2}$$

and p_{m} is the motion pressure defined as

$$-\frac{\partial p_{\mathrm{m}}}{\partial x}=-\frac{\partial p}{\partial x}+\rho_0\Omega^2 x,\quad -\frac{\partial p_{\mathrm{m}}}{\partial y}=-\frac{\partial p}{\partial y}+\rho_0\Omega^2 y$$

$$\text{and}\quad -\frac{\partial p_{\mathrm{m}}}{\partial z}=-\frac{\partial p}{\partial z}+\rho_0 g.$$

The three velocity components u, v and w are defined on the coordinates x, y and z rotating with the cavity, as shown in Fig. 1. Note that the last two terms on the right hand side of equations (2) and (3), respectively, denote the momentum change of the flow due to the Coriolis force and the centrifugal force on a variable density fluid subject to temperature nonuniformity. The corresponding initial and boundary conditions are

$$
\begin{array}{lllll}
t<0 & u=v=w=0 & \text{and}\ T=T_0 & \text{for all}\ x,y,z & \\
t\geqslant 0 & x=H/2 & u=v=w=0 & T=T_0-\Delta T/2 & \\
 & x=-H/2 & u=v=w=0 & T=T_0+\Delta T/2 & \\
 & y=\pm H/2 & u=v=w=0 & \partial T/\partial y=0 & \\
 & z=\pm H/2 & u=v=w=0 & \partial T/\partial z=0. & (6)
\end{array}
$$

In terms of the following nondimensional variables

$$X=x/H\quad Y=y/H\quad Z=z/H\quad \tau=t/(H^2/\alpha)$$
$$U=u/(\alpha/H)\quad V=v/(\alpha/H)\quad W=w/(\alpha/H)$$
$$\theta=(T-T_0)/\Delta T\quad P=p_{\mathrm{m}}/(\rho\alpha^2/H^2)$$
$$Pr=\nu/\alpha\quad Ra=g\beta\Delta TH^3/(\nu\alpha)$$
$$Ra_\omega=\Omega^2 H\beta\Delta TH^3/(\nu\alpha)\quad Ta=\Omega^2H^4/\nu^2 \tag{7}$$

the governing equations, initial and boundary conditions become

$$\frac{\partial U}{\partial X}+\frac{\partial V}{\partial Y}+\frac{\partial W}{\partial Z}=0 \tag{8}$$

$$\frac{\partial U}{\partial \tau}+U\frac{\partial U}{\partial X}+V\frac{\partial U}{\partial Y}+W\frac{\partial U}{\partial Z}$$
$$=-\frac{\partial P}{\partial X}+Pr\nabla^2 U+2Ta^{0.5}PrV-Ra_\omega X\cdot Pr\cdot\theta \tag{9}$$

$$\frac{\partial V}{\partial \tau}+U\frac{\partial V}{\partial X}+V\frac{\partial V}{\partial Y}+W\frac{\partial V}{\partial Z}$$
$$=-\frac{\partial P}{\partial Y}+Pr\nabla^2 V-2Ta^{0.5}Pr\cdot U-Ra_\omega Y\cdot Pr\cdot\theta \tag{10}$$

$$\frac{\partial W}{\partial \tau}+U\frac{\partial W}{\partial X}+V\frac{\partial W}{\partial Y}+W\frac{\partial W}{\partial Z}$$
$$=-\frac{\partial P}{\partial Z}+Pr\nabla^2 W+Ra\cdot Pr\theta \tag{11}$$

$$\frac{\partial \theta}{\partial \tau}+U\frac{\partial \theta}{\partial X}+V\frac{\partial \theta}{\partial Y}+W\frac{\partial \theta}{\partial Z}=\nabla^2\theta \tag{12}$$

$$
\begin{array}{lllll}
\tau<0 & U=V=W=0 & \text{and}\ \theta=0 & \text{for all}\ X,Y,Z & \\
\tau\geqslant 0 & X=0.5 & U=V=W=0 & \theta=-0.5 & \\
 & X=-0.5 & U=V=W=0 & \theta=0.5 & \\
 & Y=\pm 0.5 & U=V=W=0 & \partial\theta/\partial Y=0 & \\
 & Z=\pm 0.5 & U=V=W=0 & \partial\theta/\partial Z=0. & (13)
\end{array}
$$

The above formulation clearly indicates that the flow to be examined is governed by the Prandtl number Pr, Taylor number Ta, thermal Rayleigh number Ra and rotational Rayleigh number Ra_ω. Note that $Ra_\omega = Ra\cdot(\Omega^2 H/g)$. Hence the rotational buoyancy becomes important when the rotating speed is high or when cavity dimension is large, that is when Ω^2H is much larger than g.

In addition to examining the time evolution of the velocity and temperature fields, results for the local and space-average Nusselt numbers Nu and $\overline{Nu}$ on the heated or cooled plates are important in thermal design and can be evaluated from

$$Nu = -\partial\theta/\partial X|_{X=\pm 0.5} \tag{14}$$

$$\overline{Nu} = \int_{-0.5}^{0.5}\int_{-0.5}^{0.5} Nu\,\mathrm{d}Y\mathrm{d}Z. \tag{15}$$

2.2. *Solution method*

The basic equations for the present three-dimensional unsteady rotating cavity flow were solved numerically. In particular, the power-law scheme [25] was used to discretize equations (8)–(12) on a staggered grid system with the pressure and temperature defined at the mesh centers. The resulting finite difference equations were solved by the projection method [26]. To resolve the steep velocity and temperature gradients in the near-wall region, nonuniform grid was used. Specifically, the grid lines passing through the mesh centers in the X-, Y- and Z-directions were deployed as follows: $X_i = 1/2\cdot[(i-1)/i_c]^{1.5}-1/2$ for $i<i_c$ and $X_{i\max+1-i} = X_i$ for $i>i_c$; $Y_j = 1/2\cdot[(j-1)/j_c]^{1.5}-1/2$ for $j<j_c$ and $Y_{j\max+1-j} = Y_j$ for $j>j_c$; $Z_k = 1/2\cdot[(k-1)/k_c]^{1.5}-1/2$ for $k<k_c$ and $Z_{k\max+1-k} = Z_k$ for $k>k_c$, where $i$max, $j$max and $k$max are, respectively, the total numbers of the gridlines in the X-, Y- and Z-directions; i_c, j_c and k_c are the indices of the gridlines at $X = Y = Z = 0$. With those described above, the solution procedures are:

(1) Explicitly evaluate the temperature from the energy equation. To ensure numerical instability, the time interval $\Delta\tau$ must be less than $2\cdot Pr/\mathrm{MAX}(U^2, V^2, W^2)$.

(2) Calculate the provisional velocities (U^*, V^*, W^*) explicitly from the three momentum equations without the pressure gradient terms.

(3) Compute the pressure from the Poisson equation

$$\nabla^2 P = (\partial U^*/\partial X+\partial V^*/\partial Y+\partial W^*/\partial Z)/\Delta\tau$$

by the S. O. R. method. The converged pressure is reached at the mth iteration when

$$\mathrm{MAX}(|P^{m+1}_{i,j,k}-P^m_{i,j,k}|)/\mathrm{MAX}(|P^{m+1}_{i,j,k}|) \leqslant 1.0\times 10^{-4}.$$

(4) The corrected velocity (U, V, W) was calculated by correcting the provisional velocities with the pressure gradient as

$$(U-U^*)/\Delta\tau = -\partial P/\partial X$$
$$(V-V^*)/\Delta\tau = -\partial P/\partial Y$$
$$(W-W^*)/\Delta\tau = -\partial P/\partial Z.$$

(5) Repeat procedures 1–4 for each time step from the initiation of the transient to the steady state. The steady-state is considered to reach at the nth time step when

$$\mathrm{MAX}(\Psi^{n+1}_{i,j,k}-\Psi^n_{i,j,k})/\mathrm{MAX}(\Psi^n_{i,j,k}) \leqslant 1.0\times 10^{-5}$$

$$\text{and } |\overline{Nu}_{x=0.5}-\overline{Nu}_{x=-0.5}| \leqslant 1.0\times 10^{-3}$$

where Ψ stands for U, V, W or θ. For cases without steady-state, calculation is continued until a statistical state is reached.

In view of the complex flow to be simulated, stringent program tests should be conducted to verify the proposed solution method. First, computations were carried out for the limiting case of a nonrotating ($\Omega = 0$) vertical cavity. Our predicted steady local Nusselt numbers for various cases are in good agreement with the results of Bauman *et al.* [27], De Vahl Davis [28], Bajorek and Lloyd [29] and Hamady [30]. Next, tests were performed for a rotating cavity. Our predictions were compared with the experimental data of Hamady [30]. The agreement is reasonable, as exemplified in Fig. 2 for a typical case. Furthermore, results for the transient variation of the space-average Nusselt numbers on the hot wall $\overline{Nu}$ were compared with those of Fusegj *et al.* [31] in Fig. 3 for $Ra = 10^4$ and 10^6. Good agreement is noted for the entire transient. Good agreement is also noted for other flow and thermal characteristics. Finally, a grid-independence test was conducted. Results from such test for a typical case of $Ra = 10^2$, $Ta = 10^2$ and $Ra_\omega = 10^6$ are demonstrated in Table 1. The difference of the predicted maximum local velocity magnitudes $|U|_{\max}$, $|V|_{\max}$ and $|W|_{\max}$ in the three coordinate directions during the entire transient from the $30\times 30\times 30$ and $40\times 40\times 40$ grids is less than 4.2%. Better agreement is obtained for $\overline{Nu}$. The differences in $\overline{Nu}$ predicted from the $30\times 30\times 30$ and $40\times 40\times 40$ grids are within 1% during the entire transient. Furthermore, results for the velocity and temperature profiles for another typical case with $Ra = 10^6$, $Ta = 10^7$ and $Ra_\omega = 10^2$ are shown in Fig. 4. Excellent agreement is noted in the results computed from the two different grids over the entire transients. Through these tests, the proposed numerical method is considered to be suitable for the present problem.

3. RESULTS AND DISCUSSION

As indicated in the problem formulation, the flow in a differentially heated rotating cavity is governed by the Prandtl number Pr, Rayleigh number Ra, rotational Rayleigh number Ra_ω and Taylor number Ta. Although computation can be performed for any combination of these parameters, only the results required to illustrate the effects of the centrifugal and

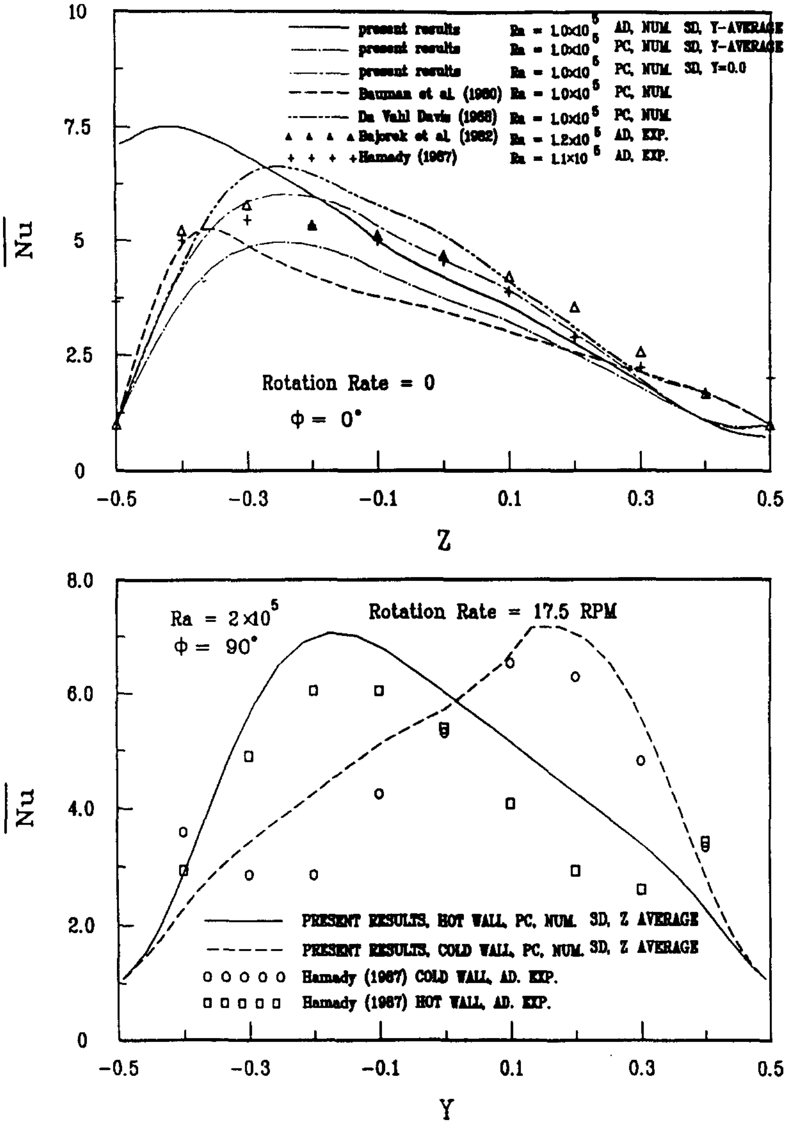

Fig. 2. Verification of steady-state Nusselt number distribution of the hot and cold walls with and without rotation.

Coriolis forces on the thermal buoyancy driven flow will be obtained in the present study. In particular, we consider air inside a rotating cubic cavity in which the rotational buoyancy and Coriolis force are systematically varied, so that they eventually dominate the flow. Specifically, Pr is set at 0.7 for air; Ra, Ta and Ra_ω are varied from 10^2 to 10^7. Only a small sample of the predicted results will be examined in the following. A detailed compilation of the complete results is available in our research report [32].

Before presenting the results for the flow driven by the interactive driving forces, the flow dominated by a single driving force is given first for comparison. Figure 5 shows the steady three-dimensional flow and temperature fields for a thermal buoyancy dominant situation with $Ra = 10^6$, $Ra_\omega = 0$ and $Ta = 0$ by plotting the velocity vectors and isotherms at selected planes, viewing from the insulated side walls of the cavity. The results indicate that the flow is mainly dominated by the strong upward and downward air streams, respectively, adjacent to the hot and cold walls, resulting in a strong clockwise flow circulation. The presence of the two insulated side walls in a cubic cavity was found to induce four weakly recirculating cells near the midheight of the cavity, which can be clearly seen by viewing the flow from the top. The resulting temperature field is of boundary-layer type and resembles that in a two-dimensional square cavity [28] except that there is some distortion in the isotherms near the insulated side walls. The corresponding local Nusselt number distributions on the hot and cold walls, not given here, showed that heat transfer is more effective in the lower portion of the hot plate and in the upper potion of the cold plate, in agreement with the directions of the boundary layer flow on these plates.

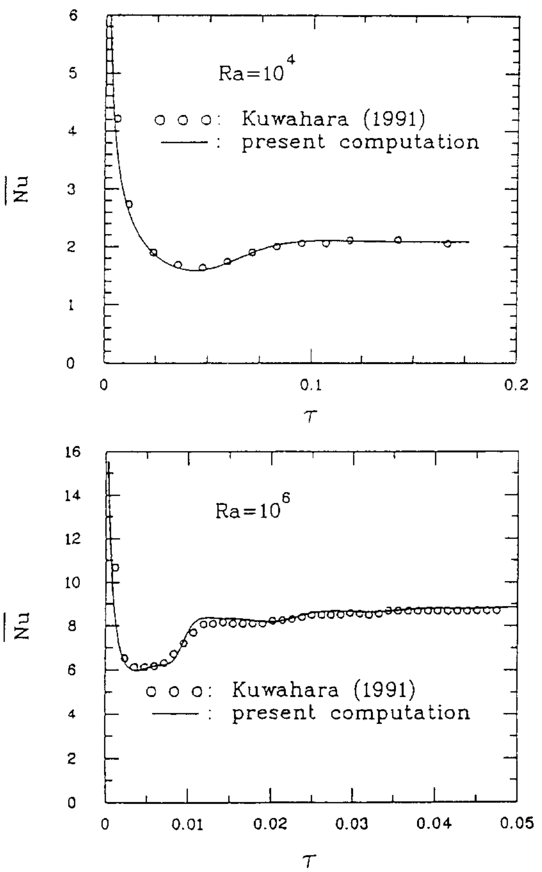

Fig. 3. Comparison of the space average Nusselt number variation with time with those of Fusegj *et al.* (1991).

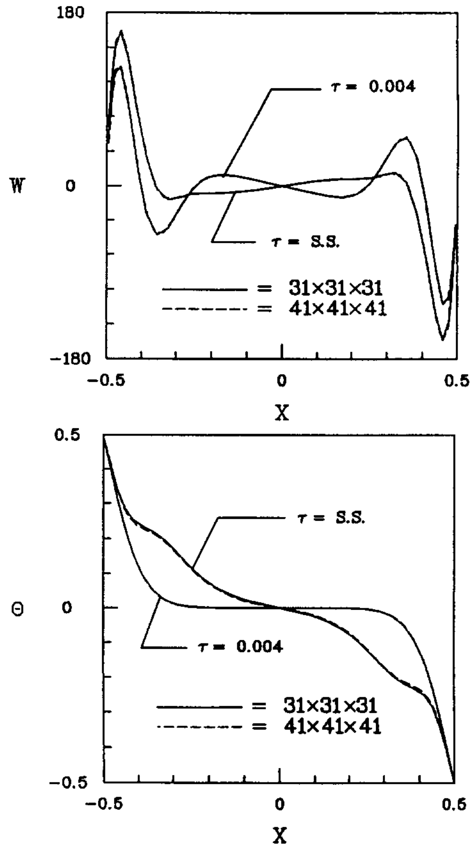

Fig. 4. Comparison of the velocity and temperature profiles along the X direction at line $Y = 0$ and $Z = 0$ computed from two different grids for a typical case $Ra = 10^6$, $Ta = 10^7$ and $Ra_\omega = 10^2$.

As the rotational buoyancy dominates over the thermal buoyancy and Coriolis force, the driven steady flow shown in Fig. 6 for $Ra = 10^2$, $Ta = 10^2$ and $Ra_\omega = 10^6$ is characterized by a pair of elongated rolls with their axes parallel with the rotating axis of the cavity, as clear by viewing the flow from the top. There is a strong stream of flow moving from the cold plate to hot plate near the insulated side walls. This unique

Table 1. Comparison of (a) the local maximum velocity magnitudes in three directions inside the cavity and (b) the space-average Nusselt numbers predicted from the 40 × 40 × 40 and 30 × 30 × 30 grid-systems for $Ra = 10^2$, $Ta = 10^2$, $Ra_\omega = 10^6$

(a)

	$\lvert U\rvert_{max}$		$\lvert V\rvert_{max}$		$\lvert W\rvert_{max}$	
τ	40 × 40 × 40	30 × 30 × 30	40 × 40 × 40	30 × 30 × 30	40 × 40 × 40	30 × 30 × 30
0.05	136.19	130.54	94.13	94.24	22.51	22.08
0.10	127.77	122.02	90.80	90.42	22.32	21.84
0.15	124.99	119.48	89.87	89.15	22.26	21.75
0.20	124.17	118.74	89.60	89.15	22.24	21.73
S.S.	123.94	118.56	89.54	89.08	22.25	21.73

(b)

	$\overline{Nu}$ at $X = -0.5$		$\overline{Nu}$ at $X = 0.5$	
τ	40 × 40 × 40	30 × 30 × 30	40 × 40 × 40	30 × 30 × 30
0.05	4.727	4.773	3.625	3.648
0.10	4.152	4.182	3.834	3.866
0.15	3.987	4.020	3.894	3.928
0.20	3.939	3.971	3.912	3.945
S.S.	3.926	3.956	3.916	3.949

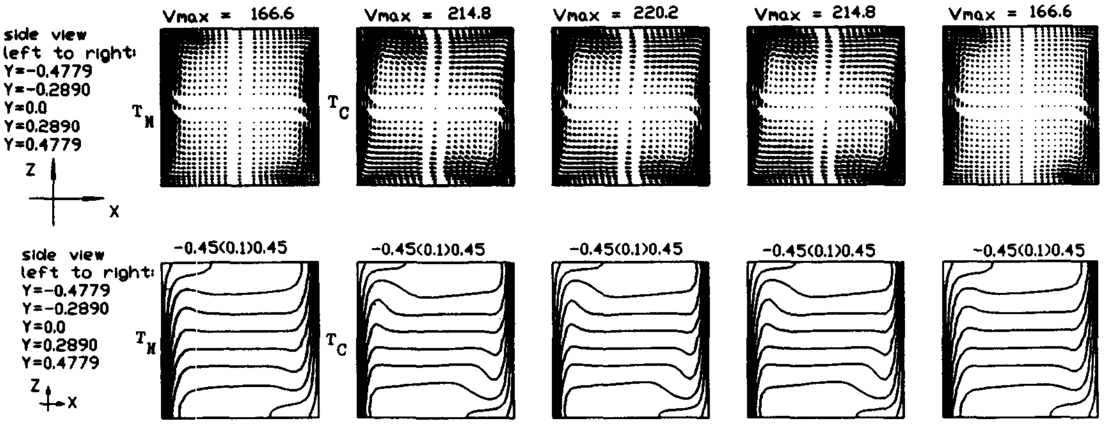

Fig. 5. The velocity vector maps and isotherms in selected planes from the side view for $Ra = 10^6$, $Ta = 0$ and $Ra_\omega = 0$ at steady state.

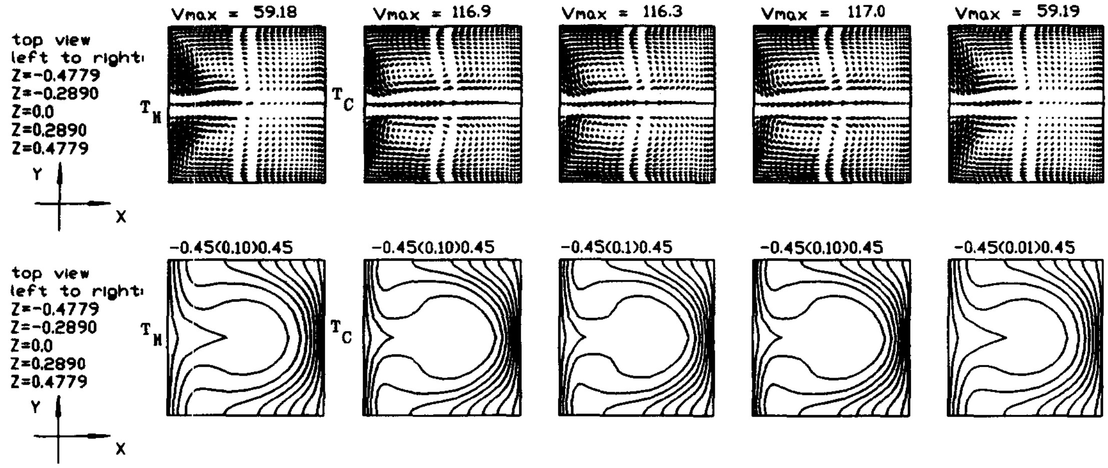

Fig. 6. The velocity vector maps and isotherms in selected planes from the top view for $Ra = 10^2$, $Ta = 10^2$ and $Ra_\omega = 10^6$ at steady-state.

flow structure results in the mushroom shape isotherms. In this Ra_ω dominated flow, the local Nusselt numbers are higher near the plane $Y = 0$ and lower near the insulated walls for the cold plate ($X = 0.5$), while they are lower at $Y = 0$ and higher near the insulated side walls for the hot plate ($X = -0.5$). For a Coriolis force dominated situation the driven flow is rather weak with $V_{\max} < 0.07$ for $Ra = 10^2$, $Ra_\omega = 10^2$ and $Ta = 10^6$.

3.1. *Effects of centrifugal force on thermal buoyancy driven flow*

To investigate the condition under which the centrifugal force exhibits significant influences on the flow driven by the thermal buoyancy, computation was performed for cases with Ra fixed at 10^6, Ta at 10^2 and Ra_ω increased from 10^2 to the level at which the flow is dominated by the rotational buoyancy. For these cases the flow was found to reach steady-state after the transient stage. The predicted results, when contrasted with those in Figs. 5 and 6, suggested that the flow is dominated by the thermal buoyancy for $Ra_\omega \leqslant 10^5$. The effects of the centrifugal force on the flow are rather slight. It is of interest to point out that the centrosymmetry of the flow is broken by this weak rotational buoyancy. As Ra_ω is raised to 10^6, the steady flow shown in Fig. 7 is still dominated by thermal buoyancy. Comparing these results with those for $Ra = 10^6$ and $Ra_\omega = Ta = 0$ in Fig. 5 reveals that in the cavity core the flow is strengthened to a certain degree by the rotational buoyancy, while the reverse is the case near the isothermal plates. Besides, the rotational buoyancy causes the boundary layer thickness on the hot and cold plates to differ noticeably. Meanwhile, it was noted that the transient time for the flow to reach steady-state is longer for a higher Ra_ω. When Ra_ω is further raised to 10^7, the flow becomes dominated by the rotational buoyancy, as supported by comparing Figs. 8 and 9 with Figs. 5 and 6. Note that at this higher Ra_ω the driven flow is again mainly in the form of a pair of vortex rolls with their axes parallel with the rotating axis of the cavity and is similar to those with $Ra_\omega = 10^6$, $Ra = 10^2$ and $Ta = 10^2$ in Fig. 6.

Next, the effects of Ra_ω on the local Nusselt number distribution on the hot ($X = -0.5$) and cold walls

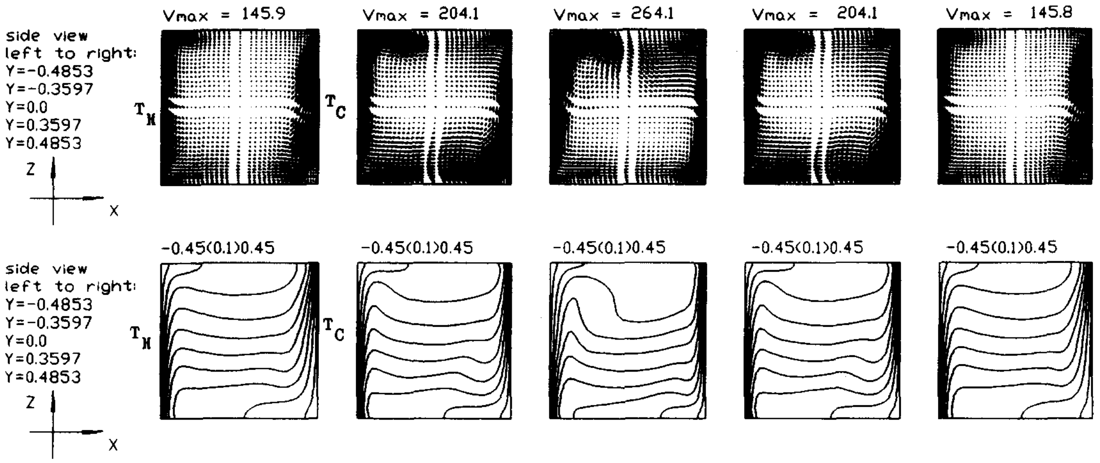

Fig. 7. The velocity vector maps and isotherms in selected planes from the side view for $Ra = 10^6$, $Ta = 10^2$ and $Ra_\omega = 10^6$ at steady-state.

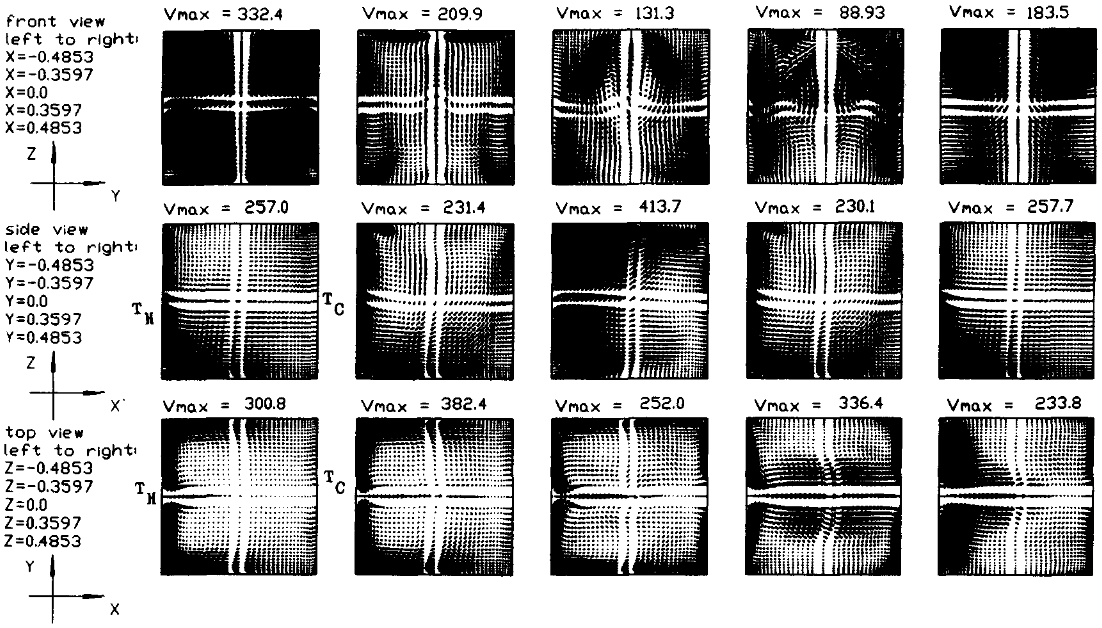

Fig. 8. The velocity vector maps in selected planes for $Ra = 10^6$, $Ta = 10^2$ and $Ra_\omega = 10^7$ at steady-state.

($X = 0.5$) are examined in Fig. 9 for $\tau = 0.005$ and for steady-state. The results indicate that at $Ra_\omega = 10^6$ the Nusselt number distributions in Fig. 10a are somewhat different from those for the thermal buoyancy driven flow, although the main flow structure is thermal buoyancy dominated, as discussed above. This is due to the fact that Nu is mainly affected by the flow near the hot and cold walls. This near-wall flow is modified to some degree for Ra_ω raised to 10^6. Very different types of Nusselt number distribution result for Ra_ω further raised to 10^7 (Fig. 10b). These distributions are not similar to those dominated by the rotational buoyancy for $Ra_\omega = 10^6$ and $Ra = Ta = 10^2$, implying that for $Ra = 10^6$ and $Ra_\omega = 10^7$ the rotational buoyancy does not predominate over the thermal buoyancy, particularly in the near-wall region. Although the rotational buoyancy exhibits significant influence on the local Nusselt number distribution, its effects on the space-average Nusselt number shown in Fig. 11 are slight, except in the initial transient.

To further illustrate the interactive effects of the thermal and rotational buoyancies on the flow, results for Ra_ω fixed at 10^6 and Ta at 10^2 with Ra varied from 10^2 to 10^7 are also examined. When $Ra \leqslant 10^5$, the flow was found to be mainly driven by the rotational buoyancy and its main structure is again in the form of a pair of vertical rolls. At $Ra = 10^6$ the resulting flow is closer to that driven by the thermal buoyancy alone, as just discussed above. As Ra is raised to 10^7, the flow is completely dominated by the thermal buoyancy. Checking the temporal flow evolution for different Ra reveals that the time for the flow to reach steady-state is shorter for a high Ra. In addition, sig-

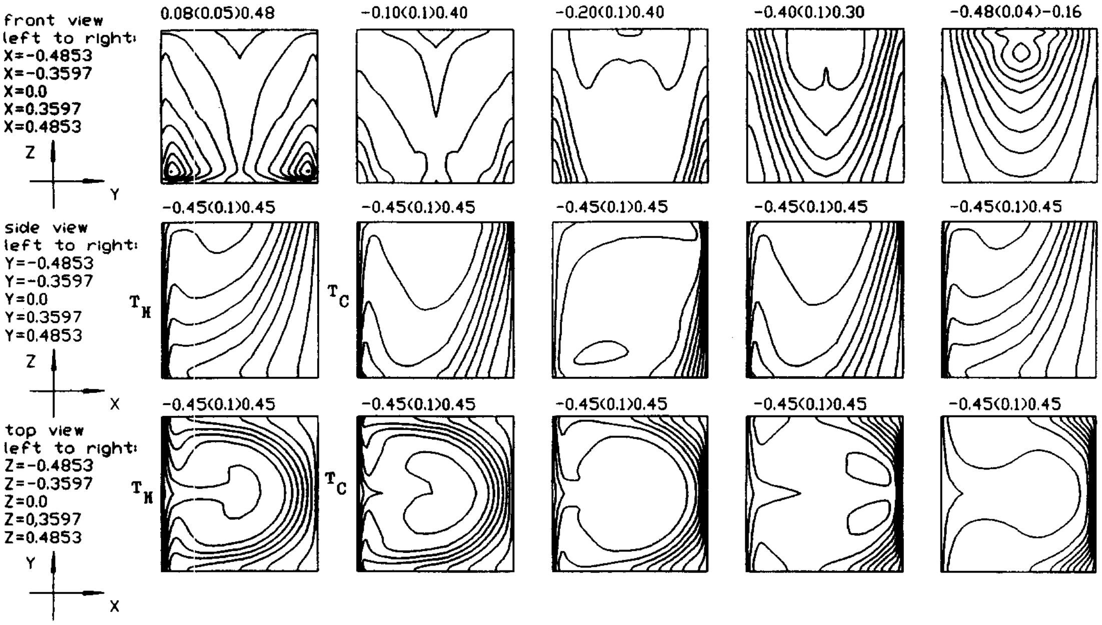

Fig. 9. The isotherms in selected planes for $Ra = 10^6$, $Ta = 10^2$ and $Ra_\omega = 10^7$ at steady-state.

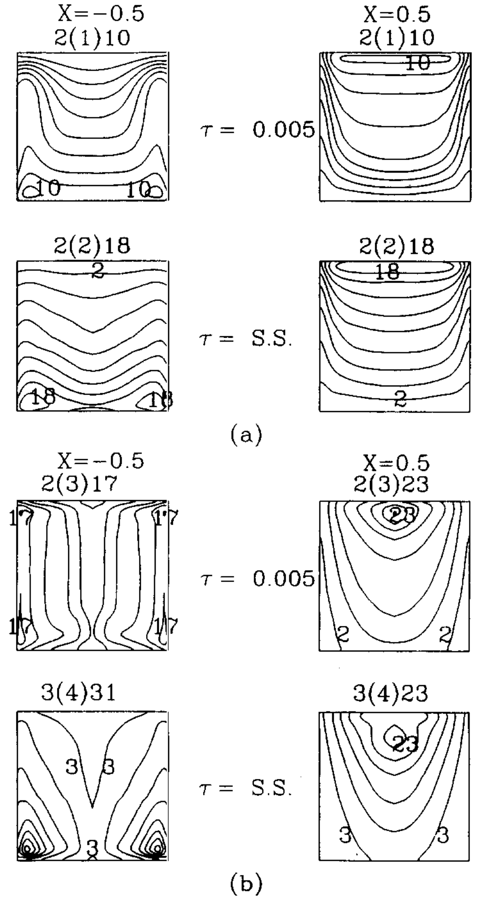

Fig. 10. The evolution of local Nusselt number distribution on hot and cold walls for (a) $Ra = 10^6$, $Ta = 10^2$ and $Ra_\omega = 10^6$ and (b) $Ra = 10^6$, $Ta = 10^2$ and $Ra_\omega = 10^7$.

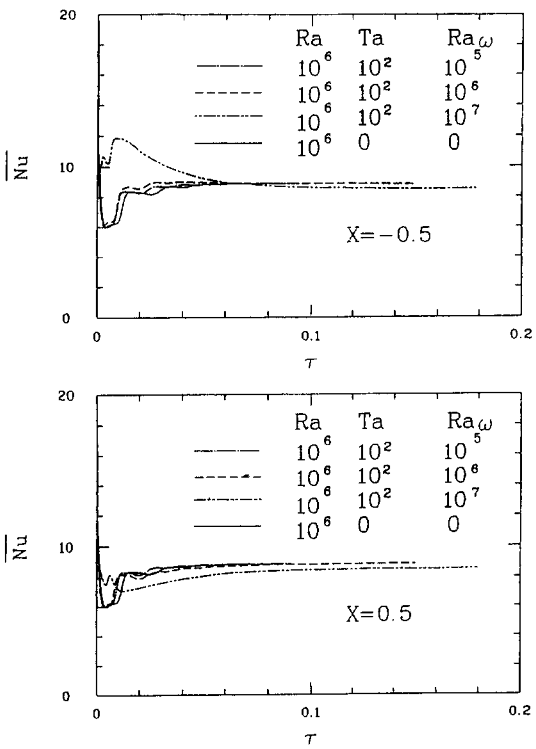

Fig. 11. The evolution of space-average Nusselt number for $Ra = 10^6$, $Ta = 10^2$ and different Ra_ω.

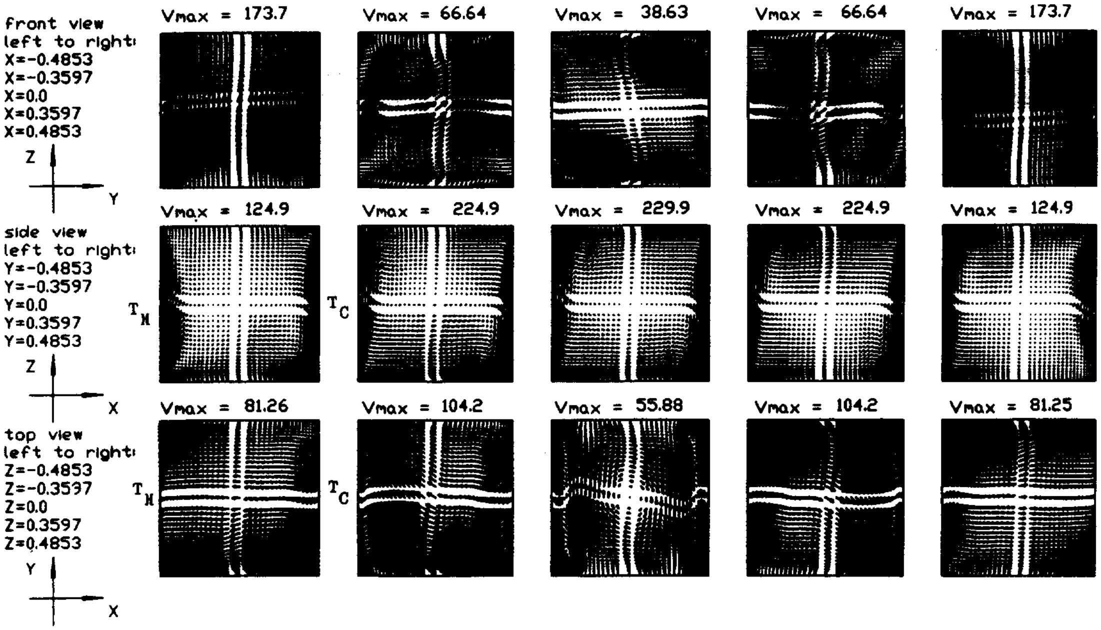

Fig. 12. The velocity vector maps in selected planes for $Ra = 10^6$, $Ta = 10^6$ and $Ra_\omega = 10^2$ at steady-state.

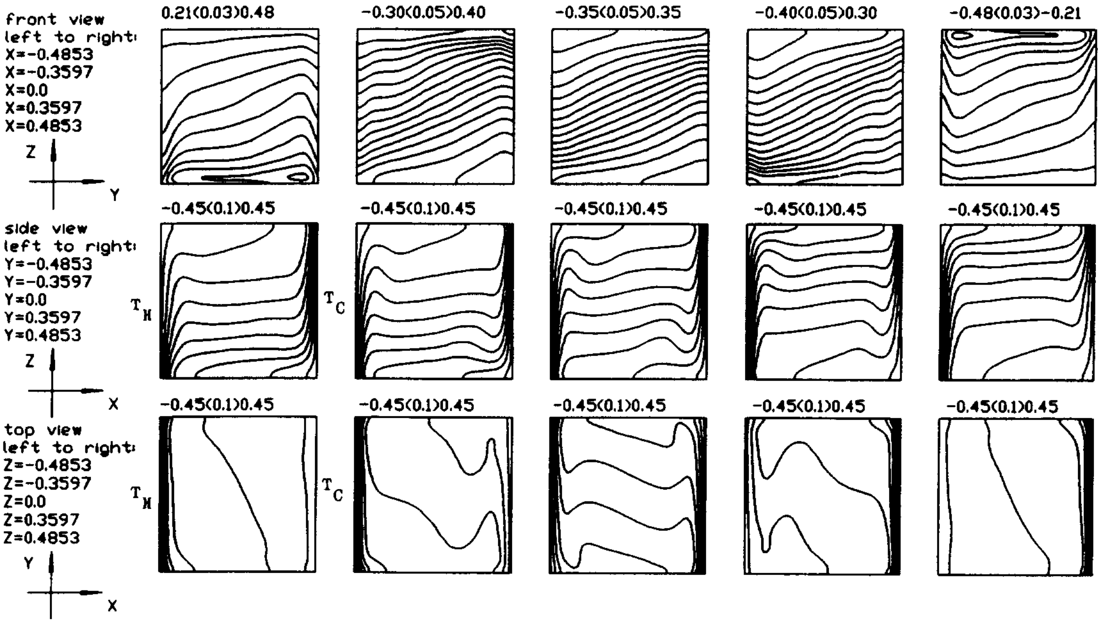

Fig. 13. The isotherms in selected planes for $Ra = 10^6$, $Ta = 10^6$ and $Ra_\omega = 10^2$ at steady-state.

nificant velocity overshoot is noted during the initial transient for $Ra = 10^6$ and 10^7. Unlike the rotational Rayleigh number, the thermal Rayleigh number shows significant influence on the space average Nusselt number. A higher $\overline{Nu}$ results for a larger Ra.

3.2. *Effects of Coriolis force on thermal buoyancy driven flow*

The interaction of the Coriolis force and the thermal buoyancy is investigated by examining the results for Ra fixed at 10^6 and Ta varied from 10^2 to 10^7 with a very small $Ra_\omega(=10^2)$. The predicted flow and temperature fields for $Ra = 10^6$, $Ta \leqslant 10^5$ and $Ra_\omega = 10^2$ suggest that the flow is close to those driven by the thermal buoyancy alone. The Coriolis force, though much smaller than the thermal buoyancy, does result in some modification in the flow and temperature fields. As Ta is raised to 10^6 with other parameters fixed at the same values, the resulting flow is found to be simultaneously affected by the thermal buoyancy and Coriolis force when the results in Figs. 12 and 13 are compared with that in Fig. 5. Although the flow structure from the side view is still similar to that in Fig. 5, the flow on the planes parallel with the hot or

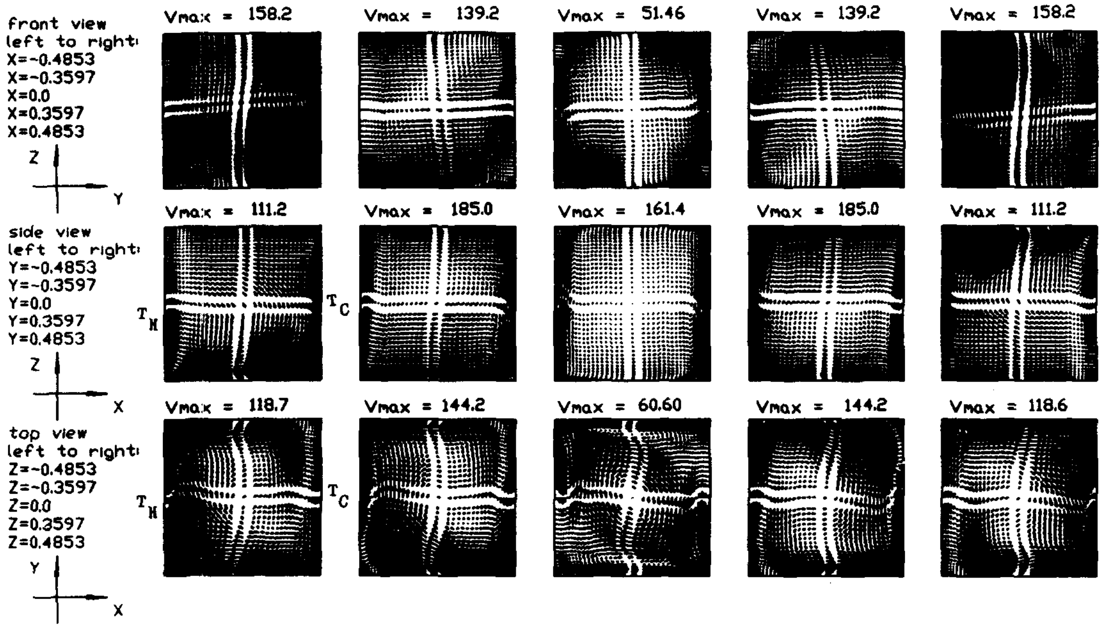

Fig. 14. The velocity vector maps in selected planes for $Ra = 10^6$, $Ta = 10^7$ and $Ra_\omega = 10^2$ at steady-state.

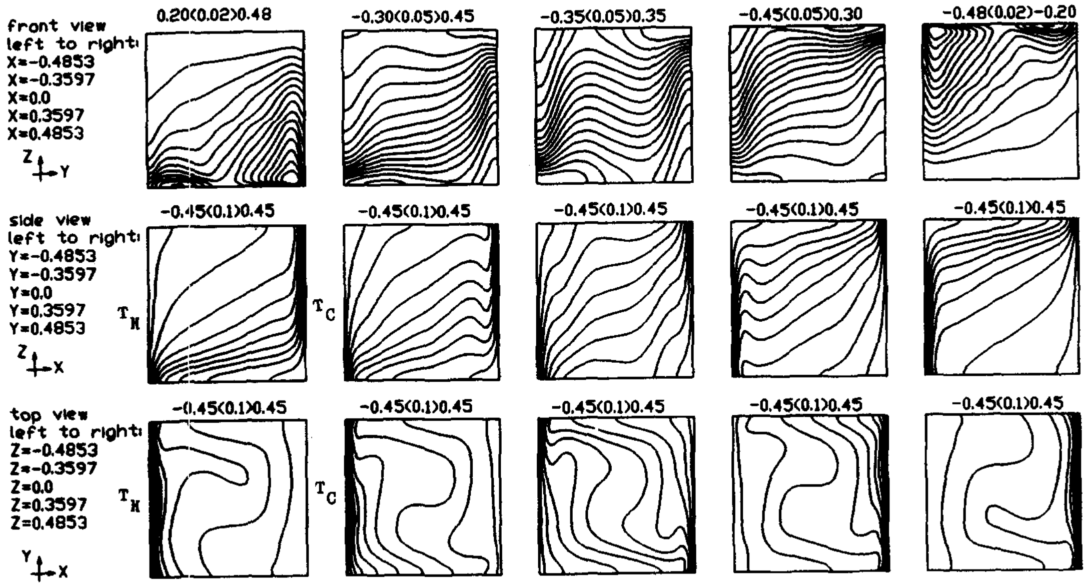

Fig. 15. The isotherms in selected planes for $Ra = 10^6$, $Ta = 10^7$ and $Ra_\omega = 10^2$ at steady-state.

cold plate (the front view) is substantially accelerated by the Coriolis force at $Ta = 10^6$ causing additional flow recirculation and distortion in the isotherms. It is also noted that the Coriolis force slightly accelerates the core flow to some degree. Besides, the boundary layers on the isothermal plates thicken slightly and the intrusion of the boundary layers along the horizontal walls is suppressed to the near-wall region for $Ta = 10^6$. Moreover, the time for the flow to reach steady-state is longer at increasing Coriolis force. For a further raise of Ta to 10^7 the flow becomes somewhat dominated and is significantly slowed down by the Coriolis force, as is clear by comparing Figs. 14 and 15 with Fig. 5. The thermal buoyancy, however, still exhibits noticeable effects because it is not small for $Ra = 10^6$. From the top view in Fig. 14 the global main steady flow structure in this Coriolis force dominated situation is in the form of four unevenly spaced vertical rolls. Besides, the time to reach steady-state was found to be shorter when Ta is raised from 10^6 to 10^7, instead of being longer.

The local Nusselt numbers displayed in Fig. 16 for various Ta indicate that increasing the Coriolis force significantly affects the local heat transfer from the

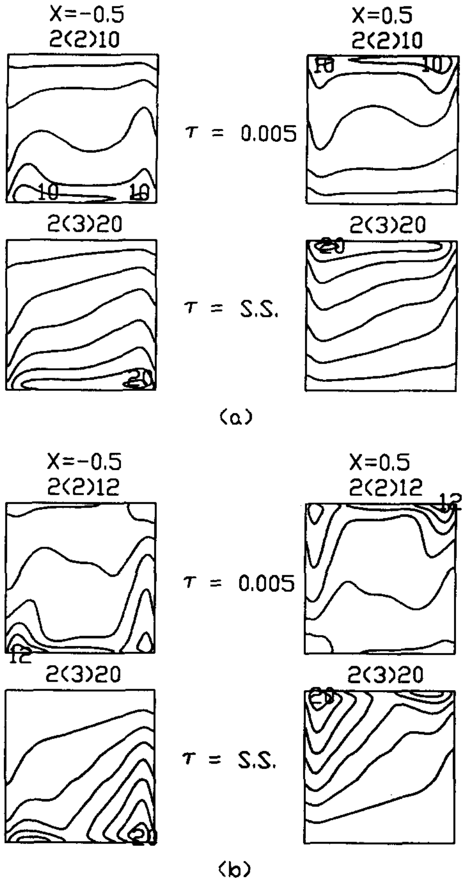

Fig. 16. The evolution of local Nusselt number distribution on the hot and cold walls for (a) $Ra = 10^6$, $Ta = 10^6$ and $Ra_\omega = 10^2$ and (b) $Ra = 10^6$, $Ta = 10^7$ and $Ra_\omega = 10^2$.

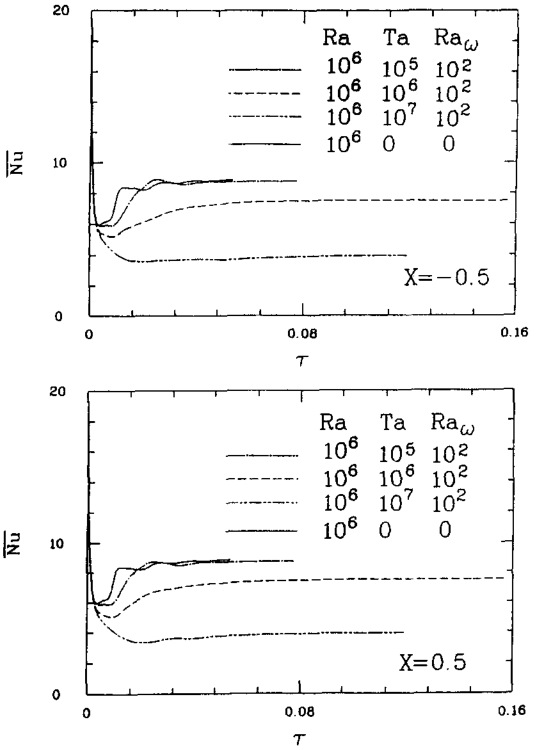

Fig. 17. The evolution of space-average Nusselt number for $Ra = 10^6$, $Ra_\omega = 10^2$ and different Ta.

hot and cold plates. The results for $Ta = 10^5$ and 10^7 are not, respectively, close to that for pure thermal convection and that dominated by the Coriolis force. The time variations of the space average Nusselt numbers presented in Fig. 17 indicate that $\overline{Nu}$ is reduced by more than 50% when Ta is raised from 0 to 10^7. This obviously results from the weakening of the thermal buoyancy driven flow near the hot and cold plates by the Coriolis force, as is clear from the side views of the results in Figs. 5 and 14.

4. CONCLUDING REMARKS

Through a detailed three-dimensional time-accurate numerical simulation, the flow structure in a differentially heated vertical cubic cavity of air is predicted. The centrifugal and Coriolis forces were found to exhibit significant effects on the flow and heat transfer in the cavity when they are high enough. In the centrifugal force dominated convection, the flow is characterized by a pair of vortex rolls with their axes parallel with the rotating axis of the cavity, resulting in the mushroom like temperature contours. The rolls are rather elongated in the direction normal to the heated wall and are divided by the vertical plane $Y = 0$. It was also found that a thermal buoyancy driven flow is strengthened at increasing centrifugal force but weakened in the near-wall regions by the increasing Coriolis force. The space average heat transfer from the isothermal plates is substantially reduced by the Coriolis force but is insensitive to the centrifugal force. The effects of the cavity inclination are unimportant in a centrifugal force dominated flow. But it is expected to cause the flow to become unstable in the thermal buoyancy and Coriolis force dominated situation. This flow transition through the Hopf bifurcation will be explored later.

Acknowledgement—The financial support of this study by the engineering division of National Science Council of Taiwan, R. O. C. through the Contract NSC 81-0401 E-009-548 is greatly appreciated. The support of the present computation by the National Center for The High-Performance computing and by the computer center of the national Chiao Tung University, Taiwan, R. O. C. is also acknowledged.

REFERENCES

1. P. P. Niler and F. E. Bisshopp, On the influence of Coriolis force on onset of thermal convection, *J. Fluid Mech.* **22,** 753–761 (1965).
2. G. Veronis, Large-amplitude Bénard convection in a rotating fluid, *J. Fluid Mech.* **31,** 113–139 (1968).
3. G. Küppers and D. Lortz, Transition from laminar convection to thermal turbulence in a rotating fluid layer, *J. Fluid Mech.* **35,** 609–620 (1969).
4. H. T. Rossby, A study of Bénard convection with and without rotation, *J. Fluid Mech.* **36,** 309–335 (1969).

5. C. Hunter and N. Riahi, Nonlinear convection in a rotating fluid, *J. Fluid Mech.* **72,** 433–454 (1975).
6. N. Rudraiah and O. P. Chandna, Effects of Coriolis force and nonuniform temperature gradient on the Rayleigh–Bénard Convection, *Can. J. Phys.* **64,** 90–99 (1986).
7. R. M. Clever and F. H. Busse, Nonlinear properties of convection rolls in a horizontal layer rotating about a vertical axis, *J. Fluid Mech.* **94,** 609–627 (1979).
8. J. L. Hudson and D. Tang and S. Abell, Experiments on centrifugal driven thermal convection in a rotating cylinder, *J. Fluid Mech.* **86,** 147–159 (1978).
9. D. Tang and J. L. Hudson, Experiments on a rotating fluid heated from below, *Int. J. Heat Mass Transfer* **26,** 943–949 (1983).
10. J. W. Chew, Computation of convective laminar flow in rotating cavities, *J. Fluid Mech.* **153,** 339–360 (1985).
11. J. C. Buell and I. Catton, Effect of rotation on the stability of a bounded cylindrical layer of fluid heated from below, *Phys. Fluids* **26,** 892–896 (1983).
12. J. M. Pfotenhauer, J. J. Niemela and R. J. Donnelly, Stability and heat transfer of rotating criogens. Part 3. Effects of finite cylindrical geometry and rotation on the onset of convection, *J. Fluid Mech.* **175,** 85–96 (1987).
13. B. M. Boubnov and G. S. Golitsyn, Experimental study of convective structures in rotating fluids, *J. Fluid. Mech.* **167,** 503–531 (1986).
14. A. G. Kirdyashkin and V. E. Distanov, Hydrodynamics and heat transfer in a vertical cylinder exposed to periodically varying centrifugal forces (accelerated crucible–rotation technique), *Int. J. Heat Mass Transfer* **33,** 1397–1415 (1990).
15. F. H. Busse, Thermal instabilities in rapidly rotating systems, *J. Fluid Mech.* **44,** 441–460 (1970).
16. F. H. Busse and C. R. Carrigan, Convection induced by centrifugal buoyancy, *J. Fluid Mech.* **62,** 579–592 (1974).
17. F. H. Busse and A. C. Or, Convection in a rotating cylindrical annulus: thermal Rossby waves, *J. Fluid Mech.* **166,** 173–187 (1986).
18. A. C. Or and F. H. Busse, Convection in a rotating cylindrical annulus. Part 2. Transitions to asymmetric and vacillating flow, *J. Fluid Mech.* **174,** 313–326 (1987).
19. L. Zhao and G. S. H. Lock, Impeded natural convection in a square tube rotating about its own axis, *Numer. Heat Transfer* **A24,** 323–338 (1993).
20. S. Abell and J. L. Hudson, An experimental study of centrifugally driven free convection in a rectangular cavity, *Int. J. Heat Mass Transfer* **18,** 1415–1423 (1975).
21. D. H. Hathaway and R. C. J. Somerville, Three-dimensional simulations of convection in layers with tilted rotation vectors, *J. Fluid Mech.* **126,** 75–89 (1983).
22. K. Bühler and H. Oertal, Thermal cellular convection in rotating rectangular boxes, *J. Fluid Mech.* **114,** 261–282 (1982).
23. S. A. Condie and R. W. Griffiths, Convection in a rotating cavity: modeling ocean circulation, *J. Fluid Mech.* **207,** 453–474 (1989).
24. G. M. Homsy and J. L. Hudson, Centrifugally driven thermal convection in a rotating cylinder, *J. Fluid Mech.* **35,** 33–52 (1969).
25. S. V. Patankar, *Numerical Heat Transfer and Fluid Flow*, pp. 90–92. Hemisphere, Washington, DC (1980).
26. M. Fortin, R. Peyret and R. Temam, *Lecture Notes in Physics*, Vol. 8, pp. 337–342. Springer, New York (1971).
27. F. Bauman, A. Gadgil, R. Kammerud and R. Greif, *Buoyancy-Driven Convection in Rectangular Enclosures: Experimental Results and Numerical Calculations.* ASME publication 80-HT-66 (1980).
28. G. De Vahl Davis, Laminar natural convection in an enclosed rectangular cavity, *Int. J. Heat Mass Transfer* **11,** 1675–1693 (1968).
29. S. M. Bajorek and J. R. Lloyd, Experimental investigation of natural convection in partitioned enclosures, *J. Heat Transfer* **104,** 527–532 (1982).
30. F. Hamady, Experimental study of local natural convection heat transfer in inclined and rotating enclosures, Ph.D. dissertation, Michigan State University, MI (1987).
31. T. Fusegj, J. M. Hyun, K. Kuwahara and B. Farouk, A numerical study of three-dimensional natural convection in a differentially heated cubical enclosure, *Int. J. Heat Transfer* **34,** 1543–1557 (1991).
32. T. L. Lee and T. F. Lin, Natural convection in inclined rotating cubic enclosure—II, Term Report of NSC 81-0401 E-009-548, Taiwan, R. O. C. (1994).